Tectonophysics 927 (2026) 231141

Contents lists available at ScienceDirect

Tectonophysics

journal homepage: www.elsevier.com/locate/tecto

Complex rupture of the 2 April 2024 M_W 7.4 Hualien earthquake inferred from seismic and geodetic observations

Ruiya Bai [a], Yingquan Sang [b,c,d], Canyang Ding [a], Chengli Liu [a,*], Lingling Ye [d], Thorne Lay [e], Neng Xiong [f], Xiong Xiong [a]

[a] Hubei Subsurface Multi-Scale Imaging Key Laboratory, School of Geophysics and Geomatics, China University of Geosciences, Wuhan, China
[b] Institute of Geology and Geophysics, Chinese Academy of Sciences, Beijing 100029, China
[c] University of Chinese Academy of Sciences, Beijing 100049, China
[d] Department of Earth and Space Sciences, Southern University of Science and Technology, Shenzhen 518055, China
[e] Department of Earth and Planetary Sciences, University of California Santa Cruz, Santa Cruz, CA, USA
[f] Department of Earth, Environmental, and Planetary Sciences, Rice University, Houston, TX, USA

ARTICLE INFO

Keywords:
2024 Hualien earthquake
Multi-fault earthquake
Geodetic and seismic observations
Finite fault inversion
Conjugate rupture

ABSTRACT

The rupture process of the 2024 Hualien M_W 7.4 earthquake was investigated through a joint inversion of seismic and geodetic datasets, revealing a complex multi-faulting event involving four fault segments that ruptured coseismically. The rupture initiated on a southeast-dipping reverse fault (F1) at a depth of 20 km. Six seconds later, slip propagated onto a conjugate reverse fault (F2), intersecting F1 at a depth of 34.5 km. Subsequent ruptures occurred on fault segments to the north; F3 at 20 s, with normal faulting mechanism, followed by overlying thrust fault F4 at approximately 33 s. The rupture propagated progressively toward the northeast, extending roughly 80 km along strike, with an average rupture velocity of ~2.5 km/s. The heterogeneous slip distributions have peak slip of ~4 m near the intersection of F1 and F2, accompanied by complementary aftershock patterns. The total seismic moment is estimated as 1.53×10^{20} N·m, with the majority released within the first 35 s, predominantly on F1 and F2. Notably, we identified depth-dependent rise time patterns on the main fault, with longer rise times at shallower depths. This study provides new insights into multi-fault interactions during a major earthquake rupture, particularly the dynamics of conjugate faulting in continental collision zones, which can guide seismic hazard assessments and more realistic simulations of complex suture zone fault behavior.

1. Introduction

Taiwan, situated along the convergent boundary between the Eurasian Plate and the Philippine Sea Plate, is a region characterized by complex tectonic interactions, making it one of the most seismically active regions globally (e.g. Tsai, 1986; Wang and Shin, 1998; Lacombe et al., 2001; Ji et al., 2003; Lo et al., 2019; He et al., 2024). The transition from mountain-building processes linked with the Central Range and Coastal Range suture zone to the subduction processes near the Ryukyu Trench has led to intense seismic activity, rapid uplift, and significant crustal deformation in the Hualien region (e.g. Yu and Kuo, 2001; Lin et al., 2010; Chen et al., 2014; Shyu et al., 2016; Lo et al., 2019). A steeply westward-dipping Central Range fault (CRF) has strike parallel to a steeply eastward-dipping Longitudinal Valley fault (LVF) along the narrow Longitudinal Valley from 22.7°N to 24.2°N, with these reverse faults bounding forearc basement and blocks of Central Range Bedrock on the Eurasian Plate and Coastal Range Bedrock on the Philippine Sea Plate (e.g., Lee et al., 2023; Tang et al., 2023).

The LVF is widely considered to be the main plate boundary, as the CRF has been less seismically active and lacks creeping deformation (e.g. Lee et al., 1998; den Hartog et al., 2021); however, the proximity and intersection of eastward and westward dipping faults at shallow depths appear to have resulted in simultaneous ruptures of both systems in recent large events, exemplified by the coseismic rupture of the 2018 M_W 6.4 Hualien earthquake (e.g. Huang and Huang, 2018; Lee et al., 2019; Lo et al., 2019; Yen et al., 2019) and the 2022 M_W 7.0 Chihshang earthquake (e.g. Lee et al., 2023; Tang et al., 2023). Near Hualien, located north of where the northern LVF, locally called the Lingding

* Corresponding author.
E-mail address: liuchengli@cug.edu.cn (C. Liu).

https://doi.org/10.1016/j.tecto.2026.231141
Received 10 October 2025; Received in revised form 20 February 2026; Accepted 24 February 2026
Available online 25 February 2026
0040-1951/

fault, trends offshore, the eastward-dipping, curved strike-slip Milun fault appears to overlie deeper westward dipping reverse faulting along offshore faults paralleling the CRF system. In addition, a series of $M \geq 5.5$ earthquakes has persisted in the northern Longitudinal Valley, near the junction between the Longitudinal Valley Suture and the Ryukyu Subduction zone, including the 18 April 2019 M_L 6.3, 15 February 2020 M_L 5.7, 18 April 2021 M_L 6.3, and 7 July 2021 M_L 5.5 events (Fig. 1; Huang and Wang, 2022), highlighting the active tectonic processes and the associated seismic hazards.

On 2 April 2024, at 23:58:12 (UTC), another major earthquake (M_W 7.4) struck the Hualien region, causing significant damage and casualties. The U. S. Geological Survey (USGS) National Earthquake Information Center (NEIC) hypocenter is 23.836°N, 121.598°E at a substantial depth of ~40 km. The *W*-phase focal mechanism suggests slightly oblique reverse faulting with best double-couple strike 19°, dip 54° and rake 73° and a notable non-double-couple component (Fig. 1) (USGS-NEIC, 2025). This is the largest earthquake on the eastern coast of Taiwan since the 1951 M_L 7.3 Hualien-Taitung earthquake (Chen et al., 2008). As reported by the Central Weather Administration (CWA) Seismological Center of Taiwan, the 2024 Hualien earthquake was followed by a strong aftershock sequence with six $M \geq 6.0$ aftershocks within the first month, including a 13.9 km deep M_W 6.4 event 13 min after the mainshock. The 2024 earthquake also triggered widespread geological hazards, including large-scale landslides, rockfalls, and slope instabilities in the steep terrain of eastern Taiwan, particularly within the Central Range and along the Suhua Highway (Chen et al., 2025). These effects differ markedly from those caused by the 2022 Chihshang strike-slip earthquake, which primarily generated surface ruptures, ground cracking, and infrastructure damage along fault traces (He et al., 2024; Hsu et al., 2024). This sequence further highlights the complex interaction between eastward- and westward-dipping fault systems in the coseismic process, reflecting the intricate structural characteristics of this collisional area (Jian et al., 2019). The USGS-NEIC assumed a single eastward-dipping model and obtained a slip distribution using strong motion data, static GNSS observations, and teleseismic body and surface waves. The model has unilateral northward propagation, with a compact main slip distribution deeper than 20 km and shallower slip likely to reach near the surface 40 to 60 km north of the hypocenter.

The 2024 M_W 7.4 Hualien earthquake provides valuable insights into the complex collisional tectonic interactions between the Eurasian Plate and the Philippine Sea Plate along eastern Taiwan, especially the activation of nearly conjugate reverse faults in the crust. This event has drawn widespread attention due to its significant implications for regional tectonics and seismic hazard. Several studies have investigated the coseismic slip distribution, with most suggesting a predominately unilateral rupture extending toward northeast. These prior investigations revealed some consistent characteristics of the earthquake but differ significantly in rupture details, highlighting the complexity and variability of the rupture (e.g. Zheng et al., 2024; Cheloni et al., 2024; Tang et al., 2025; Yang and Chen, 2025; Xu et al., 2025; Liu et al., 2025). Consequently, the rupture pattern remains debated and lacks consensus. The availability of high-quality near-field observations from the 2024 Hualien earthquake provide a rare opportunity to resolve the rupture characteristics of this event and enhance our understanding of

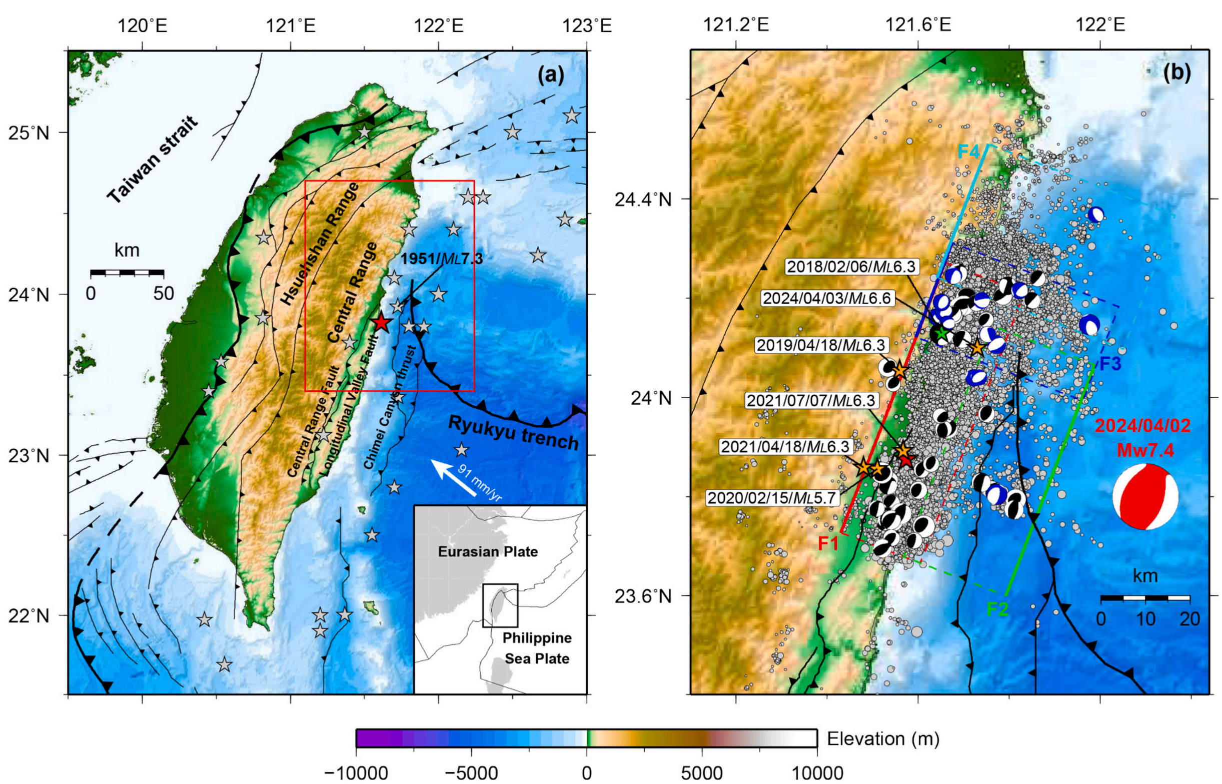

Fig. 1. (a) Tectonic setting of the 2024 Hualien M_W 7.4 earthquake. Thick black barbed lines mark the plate boundary between the Eurasian Plate and the Philippine Sea Plate, while the other thin black barbed lines indicate active faults within the plates. Red star indicates the epicenter of the mainshock. Gray stars, scaled by magnitude, show historical earthquakes with $M \geq 7.0$ from the GDMS catalog. The inset displays the general location of the study area. The white arrow indicates the convergence rate of ~91 mm/yr between the Yangtze Block of the Eurasian Plate and the Philippine Sea Plate (DeMets et al., 2010). (b) Source region of the 2024 Hualien earthquake sequence. Gray circles, scaled by magnitude, represent the relocated aftershocks within one month of the mainshock. Red star and focal mechanism are the epicenter and AutoBATS moment tensor solution (Jian et al., 2018) for the mainshock, respectively. Green star is the M_L 6.6 aftershock 13 min after the mainshock. Black focal mechanisms represent aftershocks with $M \geq 5.5$ from AutoBATS MT Catalog (Jian et al., 2018). Blue focal mechanisms indicate normal-faulting aftershocks. Orange stars denote the epicenters of damaging earthquakes ($M \geq 5.5$) in the Hualien area from 2018 to 2021. The colored dashed rectangles indicate the four mainshock fault planes used in this study, with the solid lines depicting the shallow edges. (For interpretation of the references to colour in this figure legend, the reader is referred to the web version of this article.)

damaging faulting in the region. This study seeks to integrate seismic and geodetic data to construct a unified, self-consistent model of the coseismic rupture process for this significant earthquake.

2. Data and methods

2.1. Aftershocks relocation for the 2024 Hualien sequence

To constrain the fault geometry of the 2024 M_W 7.2 Hualien mainshock, we detected and located aftershocks occurring within one month of this event. Continuous waveform data from 118 seismic stations, including 68 broadband, 30 short-period, and 20 strong-motion stations within 300 km of the epicenter, were processed following the LOC-FLOW workflow (Zhang et al., 2022) to construct a high-resolution aftershock catalog. A total of 260,659 *P* phases and 231,159 *S* phases are picked with the convolutional neural network (CNN), and we associate 16,157 events with a threshold of 15 total phases for each event. Absolute and relative relocations were performed using a 1-D velocity model averaged from the 3-D model of Huang et al. (2014) (Fig. S1). This same 1-D velocity model was also used in the subsequent finite fault inversion for calculating Green's functions. The final one-month aftershock catalog contains 14,616 events. Compared with the Taiwan Seismological and Geophysical Data Management System (GDMS) catalog, our relocated events show clearer spatial clustering, revealing detailed fault geometries reactivated during the 2024 Hualien sequence (Fig. 2).

2.2. Seismic and geodetic observations for the M_W 7.4 mainshock

The 2024 M_W 7.4 Hualien earthquake was well recorded by seismic instruments. We select strong motion records from 34 near-fault stations at epicentral distances of less than 130 km from the GDMS and P-Alert Strong Motion Network (Fig. S2). First, we remove the baseline shifts from the raw acceleration seismograms following the method of Liu et al. (2023). Then, we integrate the acceleration data to obtain ground velocity time series and apply a band-pass filter with a passband of 0.01–0.4 Hz. We calculate Green's functions for each station using the frequency-wavenumber code developed by Zhu and Rivera (2002).

We also select 54 *P* and 26 *SH* broadband teleseismic waveforms from the Incorporated Research Institutions for Seismology (IRIS) data management center, ensuring good azimuthal coverage and signal-to-noise ratio within distances of 30° to 90° (Fig. S3). Ground displacements with a duration of 70 s within the period passband of 1 to 300 s, are obtained by removing the instrument responses. Green's functions for teleseismic body waves are computed using the reflection and refraction coefficient method along with the ray theory (Helmberger, 1974).

We collect three-component coseismic displacement vectors from 70 GNSS sites operated by the Central Weather Administration of Taiwan (Fig. S2), which were processed and made accessible by the Nevada Geodetic Laboratory. Green's functions for the coseismic GNSS displacements are calculated using a generalized reflection-transmission coefficient matrix method developed by Xie and Yao (1991).

2.3. Fault geometry and inversion strategy

The cross-sectional profiles of the relocated aftershock distribution reveals evidence of multiple fault activations (Fig. 2). The spatial distribution of aftershocks delineates a complex conjugate framework: segments F1, F3, F4 and F5 are characterized as steeply eastward-dipping planes, consistent with the northern splays of the Longitudinal Valley Fault (LVF) system. In contrast, F2 represents a deeper westward-dipping reverse faulting along offshore structures paralleling the Central Range Fault (CRF) system.To explore the impact of fault geometry on the rupture process, we constructed a series of finite fault models with progressively increasing structural complexity using the hypocenter from GDMS (23.876°N, 121.574°E, 19.72 km): a single-fault model (Model I), a conjugate fault model (Model II), a three-segment model

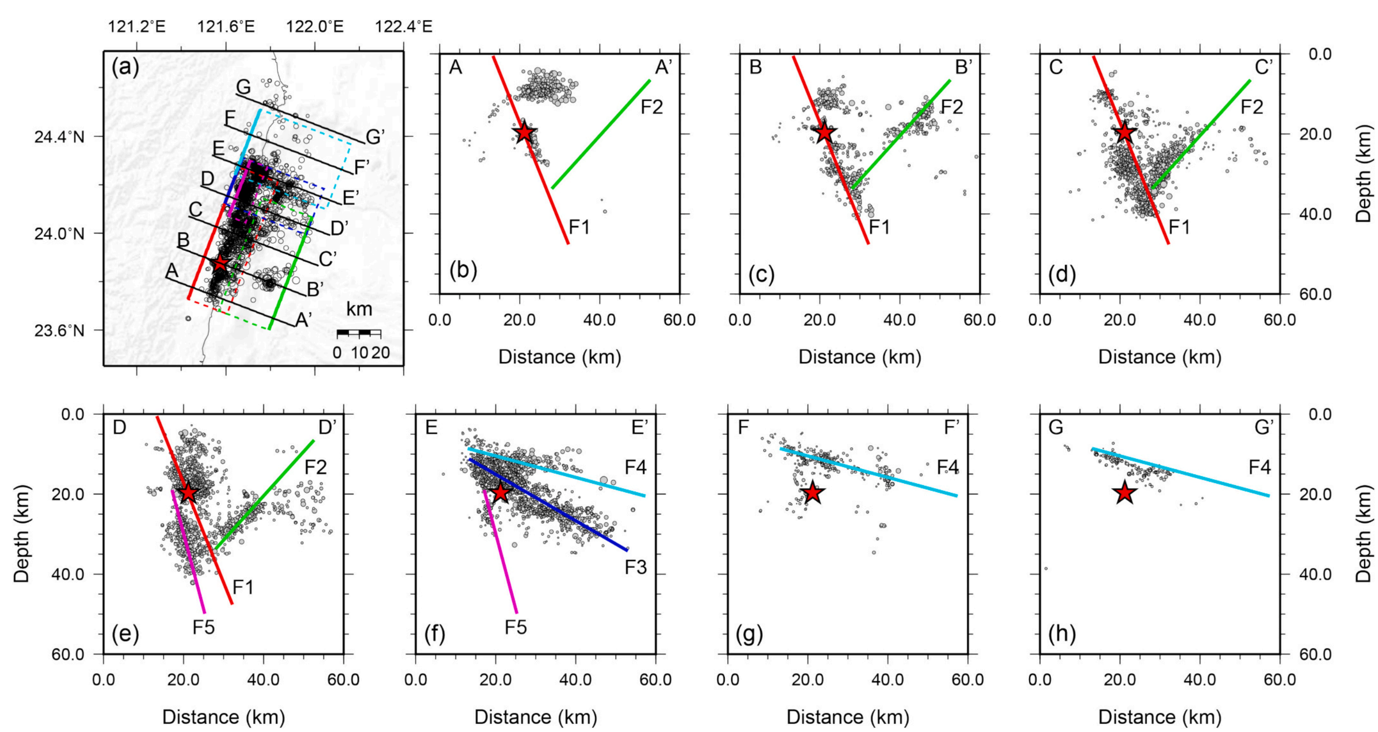

Fig. 2. (a) Map of the relocated aftershock distribution. The red star is the main shock epicenter from the GDMS. Colored rectangles indicate different fault planes used to represent the rupture geometry of the 2024 Hualien earthquake, with solid lines denoting the shallow edges of each fault. (b)-(h) denote the position and dip of the fault segments. Segment F5 does not have resolved slip during the mainshock. (For interpretation of the references to colour in this figure legend, the reader is referred to the web version of this article.)

(Model III), a four-segment model (Model IV), and a five-segment model (Model V). The parameters for all models are summarized in Table S1. These configurations allow us to systematically evaluate how different structural complexities influence the rupture behavior of the 2024 Hualien earthquake.

Using a nonlinear finite fault inversion approach, we apply a simulated annealing algorithm to simultaneously estimate the slip amplitude, rake angle, rupture initiation time, and rise time for each subfault (Ji et al., 2002, 2003). We use the following criterion to jointly invert seismic and geodetic observations: $E_{seis} + W_{st}E_{st} + W_c$ (constrains) = minimum. Two types of constraints are imposed: (1) a smoothing constraint that minimizes slip differences between adjacent subfaults, and (2) a constraint that minimizes the total seismic moment. The inclusion of these regularization terms enhances the stability of the inversion, although it may reduce the model resolution. Two weighting parameters, W_{st} *and* W_c, are introduced to balance the trade-off between fitting the two datasets and satisfying the imposed constraints. The search ranges for each parameter are provided in Table S2. To enhance the stability of the inversion, Laplace smoothing constraints are applied to both the slip distribution and rupture initiation time during the joint inversion process (Shao et al., 2011).

3. Inversion results

3.1. Evaluation of finite fault models for the 2024 Hualien earthquake

The 2024 Hualien earthquake exhibited a complex rupture pattern involving multiple fault branches, as revealed by the distribution of precisely relocated aftershocks (Fig. 2). However, it remains highly debated whether this complexity reflects a multi-segment rupture that occurred during the mainshock or the activation of secondary faults triggered by the main rupture (e.g., Zhang et al., 2012; Ruppert et al., 2018). To better understand the rupture process, we constructed and tested a series of finite fault models constrained by the spatial distribution of the relocated aftershocks, aiming to evaluate the influence of fault geometry on the rupture propagation and segmentation of the 2024 Hualien earthquake.

Model I includes only a 100-km long southeast-dipping fault (F1) with strike 21° and dip 58° toward the southeast, and closely resembles the USGS-NEIC finite fault solution (Fig. S4). This single-fault model fails to adequately explain the observed GNSS displacements, particularly near the coast (Fig. S5) and exhibits significant misfits in strong motion waveforms, particularly beyond 10 s after the rupture initiation (Fig. S6). The teleseismic waveform fits are also notably poor (Fig. S7), indicating that a single-plane fault model is insufficient to account for the rupture complexity as observed.

Model II incorporates a conjugate fault composed of a 94-km long southeast-dipping fault (F1) with strike 21° and dip 68° and a northwest-dipping fault (F2) with strike 201° and dip 48° (Figs. 2 and S8). Both faults extend along most of the aftershock zone. In this scenario, the rupture initiates on F1 and propagates to F2 after approximately 6 s, with a peak slip of ~4 m occurring at the junction of the two faults. This conjugate fault model significantly improves the fit to coseismic GNSS static displacements (Fig. S9) and teleseismic body waves (Fig. S10), and better reproduces the main characteristics of the strong motion records (Fig. S11). However, notable discrepancies remain, particularly in the high-frequency components and late cycles of the strong-motion waveforms (Fig. S11).

Model III builds on Model II by incorporating an additional 47-km long fault segment (F3) with strike 21° and dip 30° that is clearly indicated by the relocated seismicity in Fig. 2f and inferred to involve normal faulting based on the focal mechanisms of aftershocks clustered along the northeast end of F1 (Figs. 1b and S12). The model III also shortens the lengths of F1 and F2 to 65.8 km and 56.4 km, respectively (Fig. S12). The rupture initiates on the Model II versions of F1 and F2, with F3 rupturing approximately 20 s later. The rather surprising occurrence of normal faulting aftershocks within the northern end of the wedge defined by F1 and F2 is attributed to imbalance in the offsets on the thrust faults and their northern terminations which are well-constrained by relocated aftershocks (Fig. 2). The unusually shallow dip of 30° for a normal fault suggests that this may involve a reactivated thrust fault responding to the conjugate thrusting deformation to the southwest. This model results in slightly improved waveform fits for several components of the strong-motion data across multiple stations (e.g., E053, E075) (Fig. S13), and yields better agreement with teleseismic body waves compared to Model II (Fig. S14). Nonetheless, the fit to the GNSS displacements deteriorates in the northeast (Fig. S15), likely due to the lack of thrust faulting.

Model I*V* introduces a 32.9 km long thrust fault (F4) to the north of and with a gentler dip angle (15°) than a shortened version (23.5 km long) of F3, informed by the relocated aftershock distribution (Figs. 2f-h and 3). Joint inversion results reveal only minor slip on F4 (Fig. 3). The moment rate function (MRF) is similar to that of Model III, with a notable increase at approximately 35 s corresponding to the onset of F4 rupture (Fig. 3b). While this model does not significantly improve the fit to strong-motion data (Figs. 4 and S16), it achieves better agreement with the teleseismic waveforms (Fig. S17) and modest improvement in GNSS displacements fitting (Fig. 5) compared to Model III (Fig. S15).

Model *V* further incorporates a distinct fault branch with a length of 28.2 km at greater depth near the northeastern portion of fault F1, again identified in the relocated aftershock distribution (Figs. 2 and S18). This feature is added as a new segment, designated F5. Joint inversion indicates that rupture on F5 is even less prominent than on F4, with a maximum slip of only ~0.64 m, and minimal contribution to the overall rupture The corresponding data fits are shown in Figs. S19-S21. The GNSS data fitting deteriorates some in Model V (Fig. S19), indicating that the inclusion of additional minor fault branches may increase model complexity without yielding substantial improvements in data fitting, and likely represents over-parameterization of the model.

The sequence of tested models reveals that the rupture of the 2024 Hualien earthquake was governed by a complex fault system, but not all structural complexities contributed equally to the rupture process. While the single-plane fault in Model I proved insufficient to reproduce key features of all observations, the introduction of a conjugate fault system in Model II significantly improved the overall fits (Figs. S9-S11), suggesting that bilateral rupture along intersecting fault planes played a central role. Model III, which incorporates a normal fault segment (F3), further enhanced waveform fits, particularly for teleseismic and strong-motion data (Figs. S13 and S14), although it resulted in reduced accuracy in fitting some GNSS observations (Fig. S15). The addition of fault segment F4 in Model IV modestly improved GNSS and teleseismic fits but had limited impact on strong-motion waveform accuracy, indicating only minor slip involvement. Finally, Model V, which introduces a deeper branch fault (F5), resulted in minimal additional slip and a decline in GNSS fitting (Fig. S19), suggesting that this fault segment likely did not play a significant role in the main rupture. Detailed fitting errors for each model are shown in Table S3. Collectively, these models highlight that, although the 2024 Hualien earthquake involved multi-segment rupture, the primary energy release was concentrated on a few major fault planes, and adding excessive complexity to the model does not necessarily improve data fits. It is always difficult to assess the significance of added complexity in the faulting representation, but in this case the clear aftershock patterns to the north of the conjugate faults F1 and F2 provide a reasonable basis to consider the possible coseismic rupture on F3 and F4 as at least reasonable. Given the modest slip on the latter faults, and the overall improvement in fitting of some data attributes, we believe this level of complexity is justified for this well-recorded event.

3.2. Preferred rupture model

Based on the evaluation of finite fault models for the 2024 Hualien

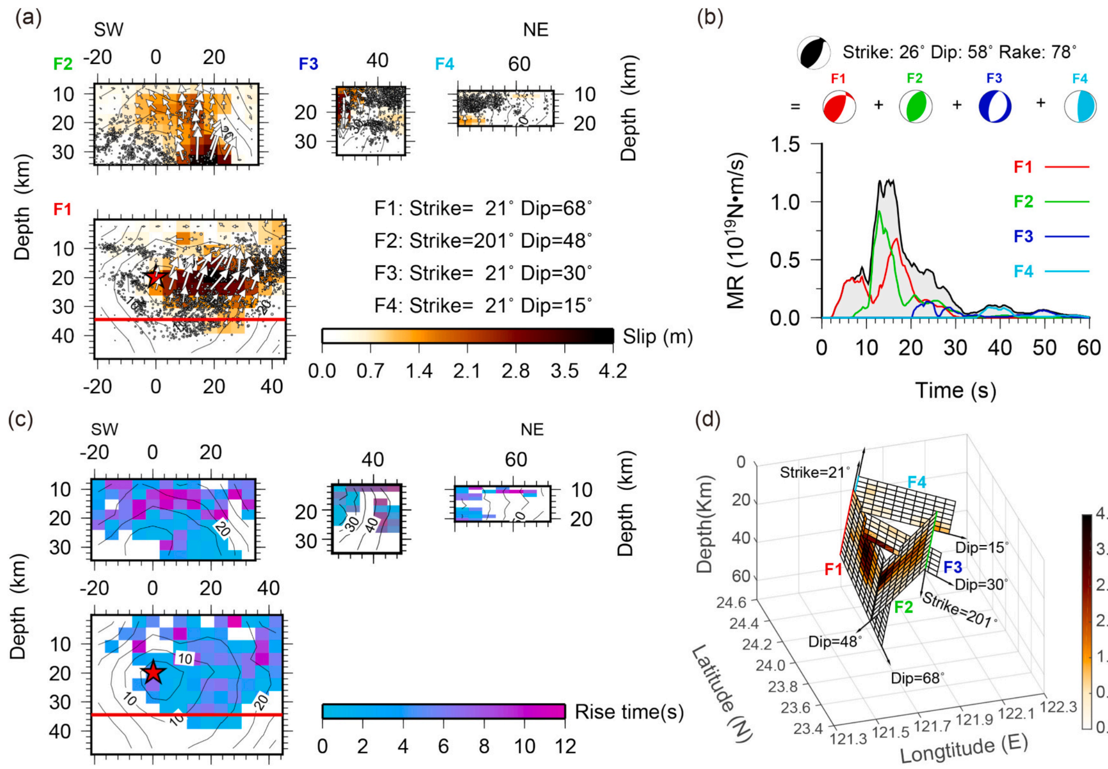

Fig. 3. (a) Preferred joint inversion results for the 2024 Hualien M_W 7.4 earthquake. The red star on F1 indicates the hypocenter. Black contours indicate the position of rupture initiation time in seconds. White arrows illustrate the variable direction of the slip on each plane. The colour bar indicates the scale for slip amplitude. The gray circles, scaled by magnitude, are the relocated aftershocks within one month. The fault geometry information of each segment is listed. (b) The moment rate function for the slip model, with colored curves representing contributions from each fault segment. The light gray-shaded region denotes the total moment rate. Moment tensors for each segment, along with the combined moment tensor (black) and the best double-couple solution, are shown at the top. (c) The distribution of rise time for the preferred slip model, excluding subfaults with slip less than 0.2 m. (d) A 3D view of the preferred slip model, with colored lines highlighting the up-dip edge of each segment. (For interpretation of the references to colour in this figure legend, the reader is referred to the web version of this article.)

earthquake, we selected Model IV as the preferred solution, as it can suitably reconcile both the seismic and geodetic datasets. The preferred four-segment slip model is shown in Fig. 3. The slip is highly heterogeneous, characterized by multiple distinct slip patches. Fig. 3b presents both the individual subfault and cumulative moment rate functions, a complex rupture process that lasted approximately 60 s with a total seismic moment of 1.53 $\times$ 10^{20} N·m, corresponding to a moment magnitude of M_W 7.4. The best-fitting double-couple solution derived from the cumulative moment tensor yields strike, dip, and rake angles of 25.6°, 58.2°, and 78.2°, respectively (Fig. 3b), generally consistent with the USGS *W*-phase solution. The preferred four-segment model provides a good fit to the coseismic GNSS displacements and teleseismic body waves (Figs. 4, 5 and S17), and it also captures the key features of the observed strong motion ground velocity records (Figs. 4 and S16). Some discrepancies remain in the high-frequency waveforms, likely due to local 3D site and path effects that are not modeled with assumed 1D velocity structure and the simplification of fault geometry using rectangular and planar faults, despite the inclusion of four distinct segments. A detailed summary of fitting errors for each dataset is provided in Table S3.

The rupture nucleated at a depth of 20 km on F1, dipping 68° to the southeast (Fig. 3). The initial rupture lasted about 6 s, and corresponds to the first peak in the MRF (Fig. 3d), characterized by a short rise time of approximately 2 s and a high slip rate of 4 m/s (Fig. 3c). Following this stage, the rupture began begain to propagate onto F2 (Fig. 6), dipping 48° to the northwest, and peaked shortly thereafter, with significant slip occurring between depths of 10 and 34 km, contributing prominently to the second peak in the MRF (Fig. 3b). Slip on both fault segments propagated unilaterally to the north. At about 20 s, rupture on the normal fault (F3) was triggered. Notably, the slip on this segment is nearly pure normal faulting, consistent with the focal mechanisms of aftershocks (Fig. 1b). The rupture lasted for about 15 s, but reactivated and ruptured after 10 s for approximately 10 s (Fig. 3b), contributing the last MRF peak between 45 s and 55 s (Fig. 3b). The rupture on F1 ceased after 30 s, while on F2, the rupture lasted for 25 s, finishing at 32 s. F4 initiated rupture at 35 s, with a relatively small slip and a short duration, contributing to the MRF peak from 35 to 44 s before halting (Fig. 3b and 6). The cumulative seismic moment at each fault segment amount to 7.96 $\times$ 10^{20} N·m (M_W 7.2), 6.2 $\times$ 10^{20} N·m (M_W 7.1), 1.99 $\times$ 10^{20} N·m (M_W 6.8), 1.12 $\times$ 10^{20} N·m (M_W 6.6), respectively. An intriguing observation is that there is a depth-dependent pattern in the rise time, with the average rise time gradually increasing from deeper regions to shallower depths (Fig. 3c).

Coseismic rupture on the complex fault segments is evidenced by both teleseismic and strong motion data, which provide complementary sensitivities to different stages of the rupture. The slip on both F1 and F2 suggests that rupture on F1 predominantly controls the initial pulse of the teleseismic *P* waves and the early local strong motion recordings (Fig. 4). However, after the first 10 s of teleseismic *P* waves, the relative contributions of F1 and F2 vary with azimuth (Fig. 4a), reflecting differences in fault orientation and slip behavior. Rupture on F1 plays a dominant role in fitting the *SH* waves, likely due to its substantial strike-slip component. Both F3 and F4, which exhibit relatively minor slip, primarily affect the strong motion recordings directly above the faults (Fig. 4b), with minimal influence on the teleseismic body waves. F3 contributes mainly to the largest phase of the teleseismic waveforms, while F4 is associated with the later phases. Synthetic waveform decompositions based on the four-segment model further illustrate how these contributions enhance the overall waveform fits (Figs. 4, S16 and S17). Overall, F1 and F2 dominate the rupture process, consistent with

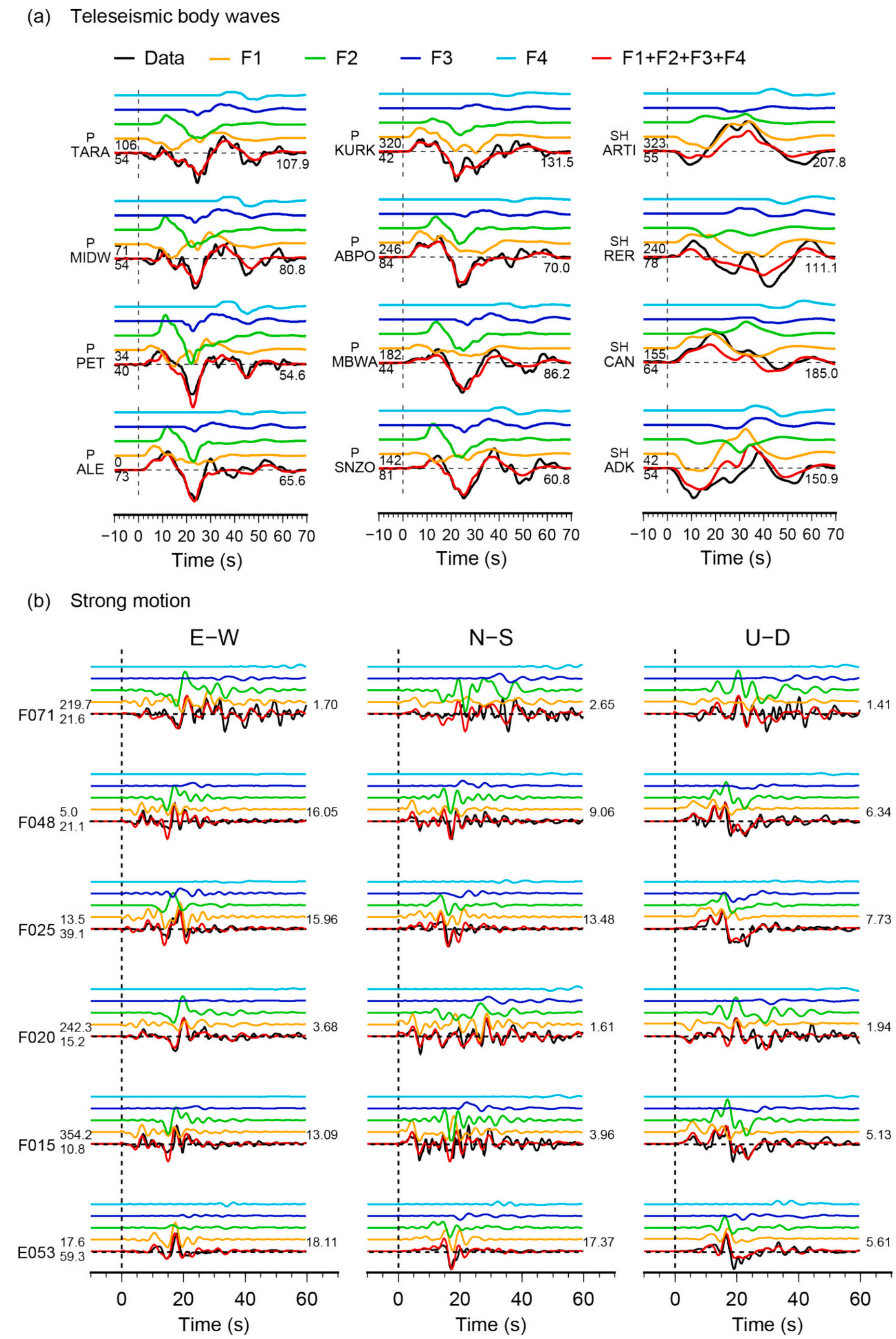

Fig. 4. Fit of selected seismic waveforms. (a) Teleseismic *P* and *SH*-wave fits between the observed data (black) and the synthetics (red). The synthetics are decomposed into contributions from F1 (orange), F2 (green), F3 (blue) and F4 (cyan). Each comparison includes the station name with distance (lower value) and azimuth (upper value) in degrees. The maximum data amplitude in micrometers is shown to the right of each comparison. (b) Three components of strong motion ground velocity waveform fits for representative stations, which are all near-fault stations. As in figure (a), the black lines represent observed data, while red line denote the sythentic predictions, with synthetics are decomposed into contributions from F1 (orange), F2 (green), F3 (blue) and F4 (cyan). The station names are shown to the left of the *E*-W component, with the maximum amplitude in the data in cm/s indicated at the right of each component. (For interpretation of the references to colour in this figure legend, the reader is referred to the web version of this article.)

the inverted slip distribution, but the contributions from F3 and F4 are non-negligible and enhance the accuracy of the inversion results. In addition, GNSS statics show excellent agreement between observed and synthetic displacements (Fig. 5), further validating the reliability of the complex rupture model.

3.3. Validation of the slip model using InSAR simulations

Our preferred four-segment slip model reveals a complex rupture process for the 2024 Hualien earthquake. While Cheloni et al. (2024) also proposed a four-segment model based on GNSS and InSAR observations, their fault configuration differs significantly from ours. Notably, their model exhibits substantial misfits between the GNSS and InSAR datasets, particularly at GNSS station HUAP, suggesting it does not fully

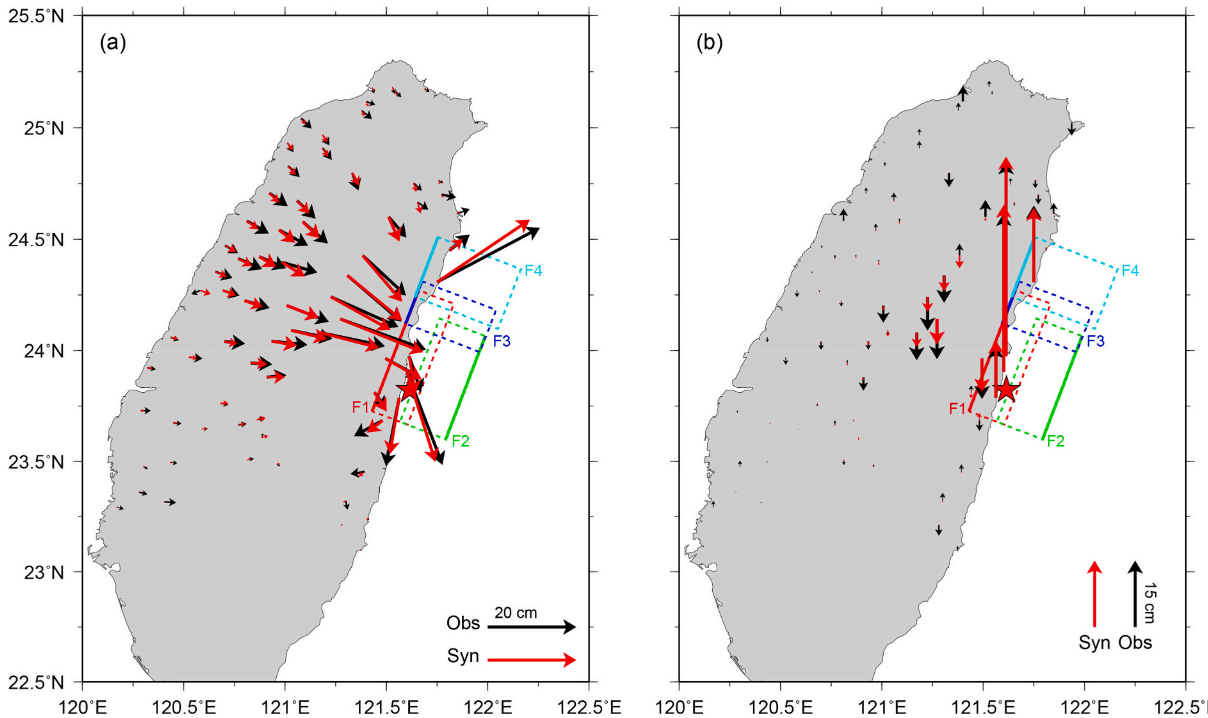

Fig. 5. Comparison between observed (black) and computed (red) static GNSS displacements for the preferred mainshock slip model shown in Fig. 3a. (a) Horizontal displacement. (b) Vertical displacement. The red-filled star indicates the epicenter of the mainshock, and the colored rectangles indicate the assumed fault planes, with the shallow edges having solid lines. (For interpretation of the references to colour in this figure legend, the reader is referred to the web version of this article.)

reconcile these two kinds of observation during the joint inversion. This highlights a common challenge in joint inversions, where the differing sensitivities, spatial resolutions, and temporal characteristics of GNSS and InSAR data necessitate careful weighting and integration.

To evaluate the consistency and reliability of our preferred model, we performed forward modeling using our preferred model to generate synthetic InSAR displacements. The simulations effectively reproduce the primary features of the observed deformation field, supporting the overall validity of our preferred slip model. However, some significant discrepancies remain near the faults. In particular, our model tends to overestimate surface displacements near the faults in the northeastern portion of the interferogram (Fig. 7), where systematic residuals exceed ~10 cm (Fig. 7c). Although the magnitude of these residuals is comparable to those in the model of Cheloni et al. (2024), our four-segment model achieves significantly better agreement with the GNSS data, especially at station HUAP.

These remaining discrepancies may be attributed, in part, to the limitations of the InSAR datasets used: ALOS-2 (L-band; ~24 cm wavelength) and Sentinel-1 (C-band; ~5.6 cm wavelength). Their spatial resolution and sensitivity may limit their ability to resolve fine-scale rupture features, particularly in areas of steep deformation gradients or decorrelation. These limitations, along with the potential influence of early postseismic deformation and shallow aftershocks, likely contribute to the residuals.

By incorporating high-quality seismic and coseismic GNSS statics in the joint inversion and using InSAR observations independently for validation, we demonstrate that our four-segment model guided by the aftershock distribution is both physically plausible and consistent with the key features of the surface deformation. This approach enhances confidence in our interpretation of the rupture process, and mitigates the potential biases introduced by joint inversions when observation types are not fully compatible.

3.4. Evaluation of model uncertainty

To evaluate the uncertainty of the slip model for the 2024 Hualien earthquake, we conducted ten inversions using different random seeds. This procedure allows us to quantify the uncertainty associated with multiple possible optimal solutions in the model space. The results show that the regions of large slip are highly consistent across all models, underscoring the robustness and stability of both the coseismic slip pattern and the moment rate function (Fig. S22a). The slip standard deviation (STD) is generally small (<10%) across most of the fault surface (Fig. S22b), although the average slip STD of individual subfaults increases with depth. Elevated STD values observed on fault segment F3 and at the junction between F1 and F2 likely reflect reduced model resolution in these areas and trade-offs in slip partitioning between adjacent fault segments.

4. Discussion

4.1. Comparison with published rupture models

Compared to previously published rupture models, our preferred four-segment slip model provides a more comprehensive and physically robust representation of the 2024 Hualien earthquake rupture. Zheng et al. (2024) conducted a joint inversion of seismic and geodetic data, identifying a compact slip distribution on a southeast-dipping, listric fault. Tang et al. (2025) proposed a simple low-angle fault model based on GNSS and InSAR data, suggesting that the slip was concentrated at depths of 10–33 km and was dominated by reverse motion with a minor strike-slip component. However, their models neglect the rupture complexity suggested by aftershock patterns and fails to capture detail slip contributions. Cheloni et al. (2024) adopted a four-segment fault geometry guided by aftershock distributions, achieving better fits to geodetic data and effectively capturing distributed slip across multiple fault structures, but their slip distribution differs significantly from our preferred model. Yang and Chen (2025) analyzed strong-motion

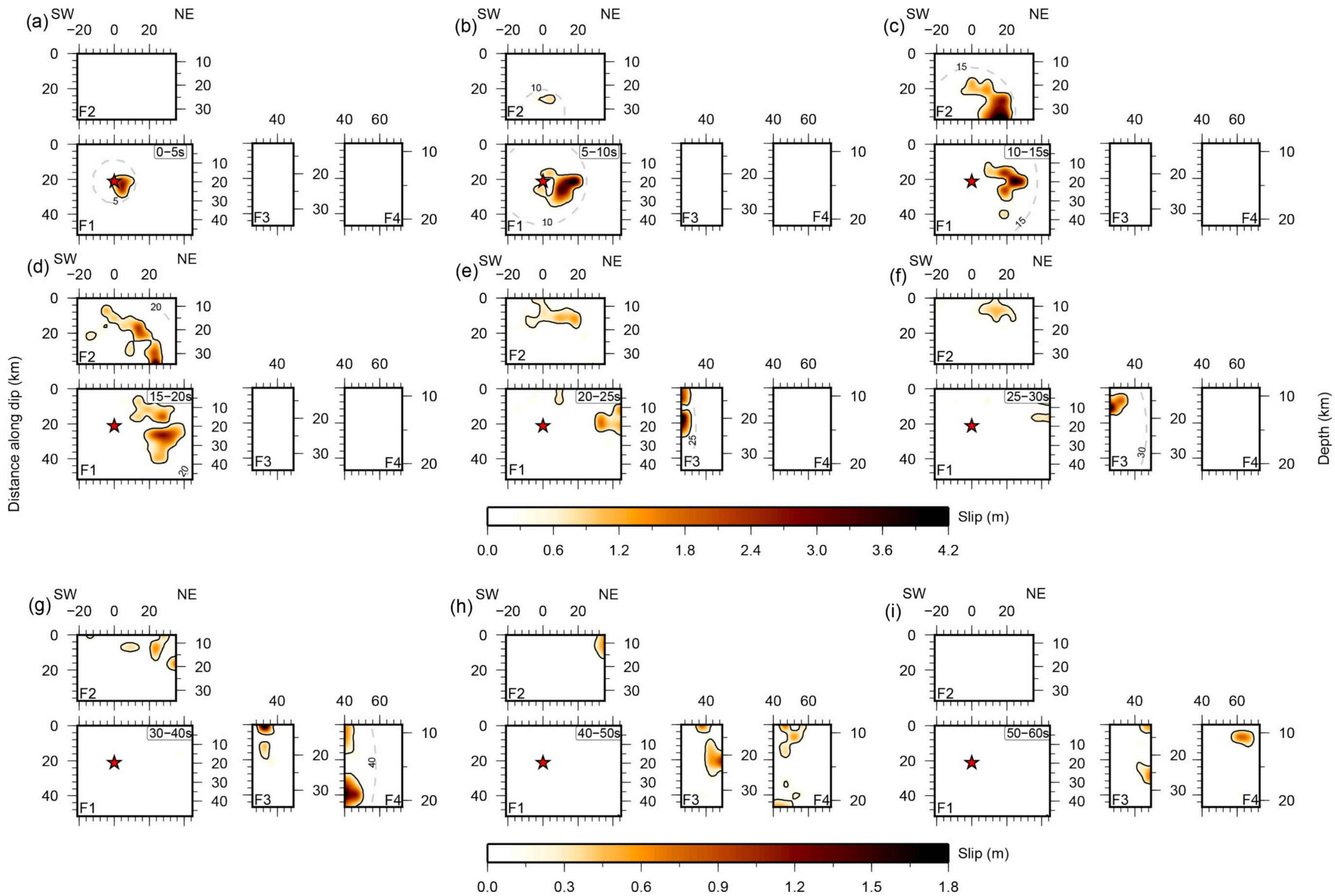

Fig. 6. Snapshots of the rupture history for the 2024 M_W 7.4 Hualien earthquake with a time interval of 5 s for the first 30 s and 10 s for the subsequent 30 s. The gray dashed contour denotes the position of a reference rupture front with a rupture velocity of 2.5 km/s, and colors indicate the slip magnitude. To better illustrate the slip distribution, different colorbar scales are used. Gray solid contours highlight regions where the slip exceeds 0.2 m.

waveform data and derived a rupture model featuring predominantly unilateral rupture toward the NNE, with the main slip occurring at depths of ~41–49 km and a peak slip of 2 m, this potentially influenced by the deep rupture initiation they used. Xu et al. (2025) tested a series of model candidates and ultimately proposed a conjugate rupture scenario, in which rupture propagated from the east-dipping Longitudinal Valley fault to the west-dipping fault, with the peak slip on the west-dipping fault, consistent with our preferred model. Liu et al. (2025) also suggested a conjugate rupture model by jointly inverting seismic and geodetic observations. However, their solution differed from that of our preferred model and Xu et al. (2025) in strike orientation and hypocenter depth, resulting in a distinct slip distribution. Moreover, their model failed to adequately reproduce the horizontal GNSS displacements and teleseismic body waves, raising concerns about its reliability. In contrast, our model is constructed using relocated aftershocks and integrates high-quality seismic and coseismic GNSS displacements through a joint inversion, with independent validation from InSAR observations. It successfully captures the segmented slip pattern, providing a kinematically consistent scenario of the complex rupture process.

4.2. Relationship between mainshock rupture and aftershock distributions

The 2024 Hualien M_W 7.4 earthquake was followed by a substantial number of aftershocks (Figs. 1 and 2), providing an important dataset to examine the relationship between coseismic rupture and subsequent seismicity. We compared the coseismic slip distribution of our preferred slip model with the spatial distribution of relocated aftershocks ($\geq M$ 2.0) (Fig. 3a). The aftershocks are predominantly shallow, with most events occurring above 30 km depth, and are strongly clustered around the edges of the high-slip patch on both F1 and F2, showing a notable complementarity with the coseismic rupture zone (Fig. 3a), consistent with stress transfer and rupture arrest at fault boundaries (e.g., King et al., 1994; Woessner et al., 2006). A similar relationship is observed on both F3 and F4, where aftershocks tend to surround the main asperities rather than directly overlapping them. Notably, regions exhibiting low slip and sparse aftershock activity may represent rupture barriers, where structural or frictional heterogeneities inhibit rupture propagation and could serve as nucleation zones for future earthquakes (e.g., Kaneko et al., 2010; Michel et al., 2019). The limited number of moderate-to-large aftershocks within the main high-slip areas suggests that the coseismic rupture released a substantial portion of the accumulated stress. This observation is consistent with patterns seen in other large continental earthquakes and indicates a relatively efficient stress drop during the rupture (e.g., Wetzler et al., 2016; Yoshida et al., 2016).

4.3. Rupture initiation and the development of the conjugate rupture

Numerous studies have documented the rupture of conjugate fault structure during earthquakes (e.g., Robinson et al., 2001; Aochi and Kato, 2010; Yue et al., 2012; Fukuyama, 2015; Lay et al., 2018), particularly within strike-slip fault systems. In contrast, coseismic ruptures involving conjugate reverse faults are relatively rare (e.g., Kato et al., 2008; Yoshida et al., 2014; Fig. S23), highlighting the unique mechanical and geological conditions that govern their activation during seismic events. Dynamic simulations by Aochi and Kato (2010) demonstrated that rupture transfer along overlapping segments of

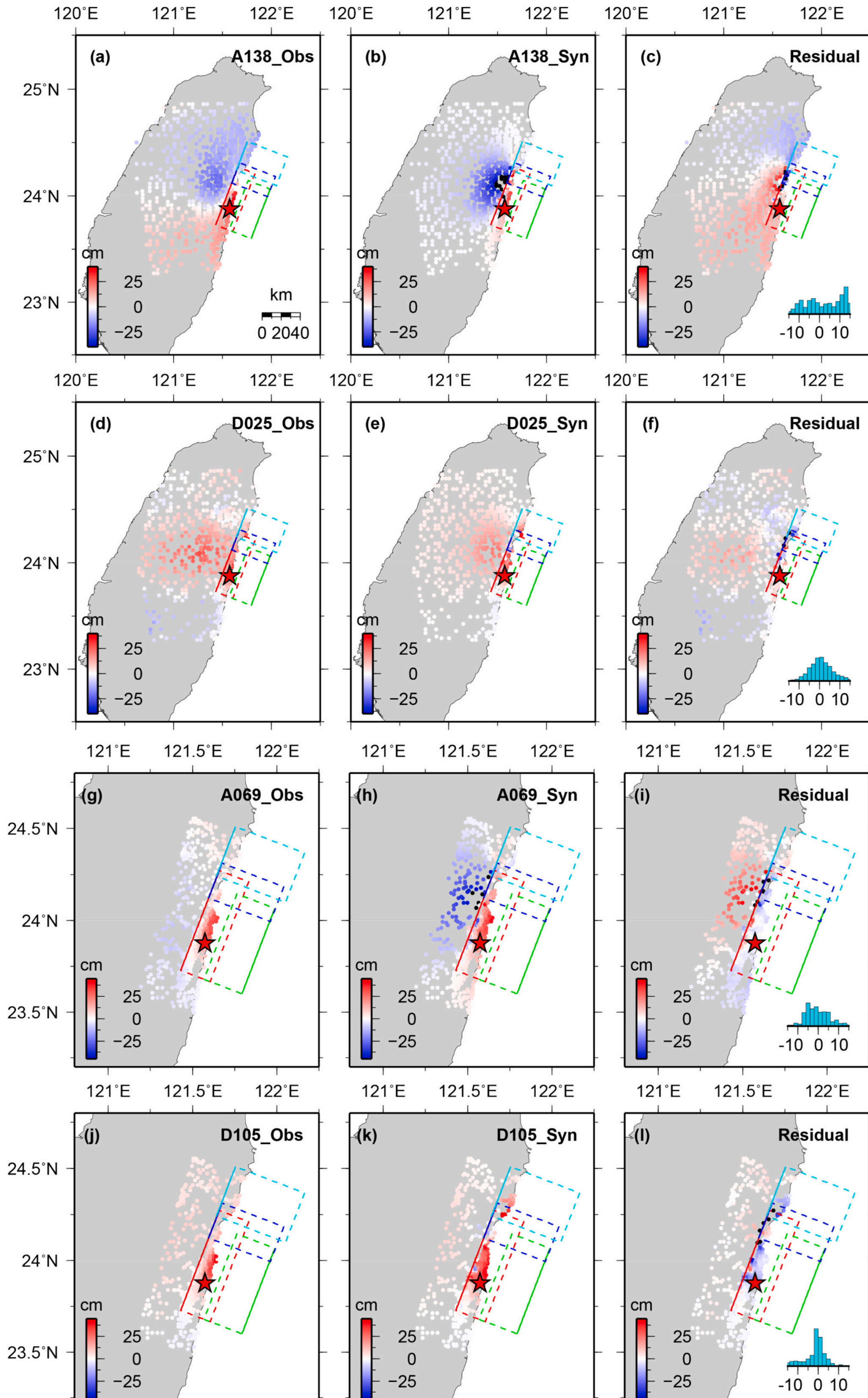

Fig. 7. Line-of-sight (LOS) displacement fields and synthetics. (a), (d), (g) and (j) LOS displacements for the ALOS-2 and Sentinel-1 from Cheloni et al. (2024). (b), (e), (h) and (k) Prediction of LOS displacements using the our preferred slip model in Fig. 3. (c), (f), (i) and (l) Residuals of each track of LOS displacements. Statistical histograms indicate the distributed residuals. The colored rectangles show the fault planes, and the star is the epicenter of the mainshock.

conjugate faults is possible, though highly sensitive to prevailing frictional and stress conditions (Freed, 2005).

To quantitatively investigate the interaction between conjugate faults, we construct a simplified fault model to calculate the static stress changes on F2 induced by early slip on F1, using the PSGRN/PSCMP program (Wang et al., 2006), with variable rupture initiation points. Our results show that the location of the rupture initiation point on F1 significantly affects the potential for triggering rupture on F2 (Fig. 8). When rupture initiates above or at the intersection of the two faults, it induces a positive Coulomb failure stress (CFS) change on Fault F2 (Fig. 8a and b), promoting rupture propagation. In contrast, initiation below the intersection leads to a reduction in CFS on F2, thereby inhibiting rupture initiation (Fig. 8c).

These findings are consistent with previous dynamic simulations, which show that rupture initiating at the intersection and propagating bilaterally can trigger the second fault within a few seconds (Aochi and Kato, 2010). This is also supported by the 2024 M_W 7.4 Hualien earthquake, during which the first 6 s of rupture on F1 significantly increased the CFS on F2 (over 10 MPa) at locations corresponding to the nucleation and main slip areas of our preferred model (Fig. 8d), indicating that these regions were brought closer to failure. This also suggests that the rupture nucleation depth on F2 was not extremely shallow. The short and high slip rate at the initial 6 s on F1 found in our preferred slip model also promote the cascading failure on the both conjugate fault planes dynamically.

Overall, this analysis provides quantitative insight into how slip on one fault can change stress conditions and influence rupture behavior on its conjugate fault. It underscores the complex dynamic interactions possiblity during reverse faulting earthquakes, and contributes to improved assessments of potential rupture scenarios, thereby enhancing earthquake hazard evaluation and mitigation strategies in compressional mountain settings.

4.4. Seismological metric for the complex rupture: E_r/M_0

The ratio of radiated energy to seismic moment is a key parameter in earthquake studies (e.g., Venkataraman and Kanamori, 2004; Convers and Newman, 2011; Ye et al., 2016). The total broadband radiated elastic energy (E_r) estimated with teleseismic body waves for the 2024 Hualien earthquake is 3.3×10^{15} J. Our joint inversion yields a total seismic moment of $M_0 = 1.53 \times 10^{20}$ N·m. The ratio of radiated energy to seismic moment, $E_r/M_0 = 2.2 \times 10^{-5}$, moderately exceeds the global

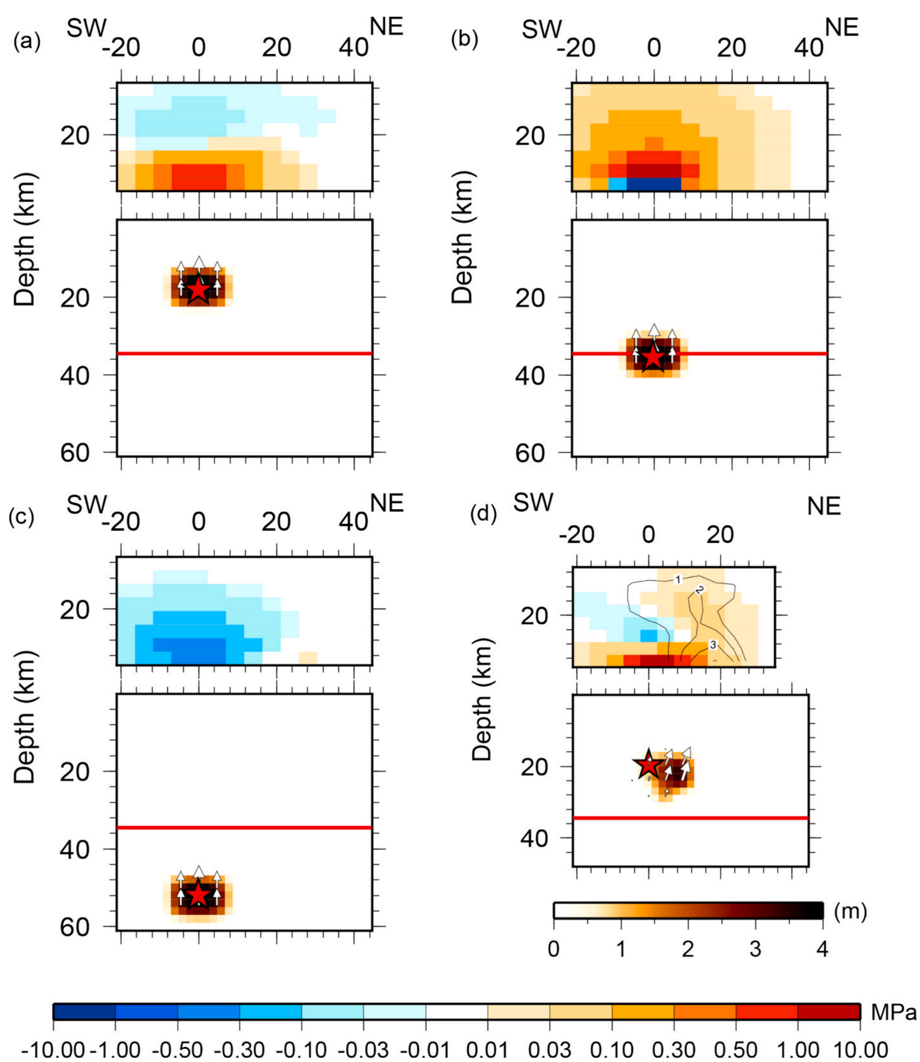

Fig. 8. Coulomb stress change tests on fault F2 induced by preceding slip on fault F1 for various nucleation points in a conjugate fault system. The red star marks the assumed hypocenter in each scenario, and the red line indicates the intersection of the two faults. (a) Nucleation located above the fault intersection. (b) Nucleation located at the fault intersection. (c) Nucleation located below the fault intersection. (d) Calculations for the first 6 s of slip in our preferred rupture model. Black contours indicate the total slip distribution on F2 for the preferred slip model shown in Fig. 3a. (For interpretation of the references to colour in this figure legend, the reader is referred to the web version of this article.)

average for interplate thrust earthquakes (1.06×10^{-5}; Ye et al., 2016). This somewhat high E_r/M_0 ratio might correspond to the short rise times observed at deeper depths (Fig. 9), indicating efficient conversion of accumulated tectonic energy into seismic waves during the coseismic process. This resulted in strong ground shaking near the epicenter, as reported by the Central Weather Administration Seismological Center of Taiwan.

We compiled a global dataset of large earthquakes that exhibit complex rupture behavior, including rupture across multiple fault segments and rupture branching. Based on published finite-fault models and estimates of teleseismic radiated energy from IRIS, we calculated the ratio of radiated energy to seismic moment (E_r/M_0) for each event. Detailed parameters are shown in Table S4. The results show that earthquakes with complex rupture geometries generally have significantly higher E_r/M_0 ratios than the global average for interplate thrust events and are often comparable to those of strike-slip earthquakes (Fig. 9; Ye et al., 2016; Liu et al., 2023). This observation supports the interpretation that rupture complexity enhances high-frequency radiation, likely due to rapid stress variations and heterogeneous slip evolution during rupture propagation (Mai and Beroza, 2002; Dunham et al., 2011).

For the 2024 Hualien earthquake, rupture across multiple fault segments likely introduced substantial dynamic complexity, facilitating enhanced seismic energy radiation relative to the total moment release. This highlights the critical role of rupture geometry and fault interactions in governing earthquake energy budgets and associated ground motion characteristics.

5. Conclusions

This study presents a comprehensive analysis of the 2024 M_W 7.4 Hualien earthquake, revealing an exceptionally complex rupture process involving the coseismic activation of a conjugate fault system and additional segments, a phenomenon rarely documented for reverse faulting events. Our preferred finite-fault model (Model IV), constrained by high-resolution aftershock relocation and jointly inverted from seismic and geodetic data, reveals that the rupture nucleated on a steeply southeast-dipping fault (F1) and dynamically triggered rupture on its conjugate northwest-dipping fault (F2) within seconds. This bilateral rupture was followed by subsequent, smaller-magnitude slip on a normal fault (F3) and a shallow thrust fault (F4). The majority of the seismic moment was released on the conjugate faults F1 and F2, with slip distributions that are spatially complementary to the aftershocks, indicating stress transfer to the edges of the main rupture. Complex multi-segment rupture can result in a higher-than-average radiated energy to seismic moment ratio ($E_r/M_0 = 2.2 \times 10^{-5}$), a characteristic of geometrically complex earthquakes wordwide that efficiently generate high-frequency radiation. This earthquake highlights the critical influence of intricate fault zone geometry in compressional tectonic settings on earthquake dynamics, energy partitioning, and associated seismic hazard.

CRediT authorship contribution statement

Ruiya Bai: Investigation, Formal analysis, Data curation. **Yingquan Sang:** Investigation, Formal analysis, Data curation. **Canyang Ding:** Investigation, Formal analysis, Data curation. **Chengli Liu:** Writing – original draft, Methodology, Investigation, Funding acquisition, Formal analysis, Data curation, Conceptualization. **Lingling Ye:** Writing – original draft, Methodology, Investigation, Funding acquisition, Formal analysis, Data curation. **Thorne Lay:** Writing – original draft, Investigation, Funding acquisition, Formal analysis, Conceptualization. **Neng

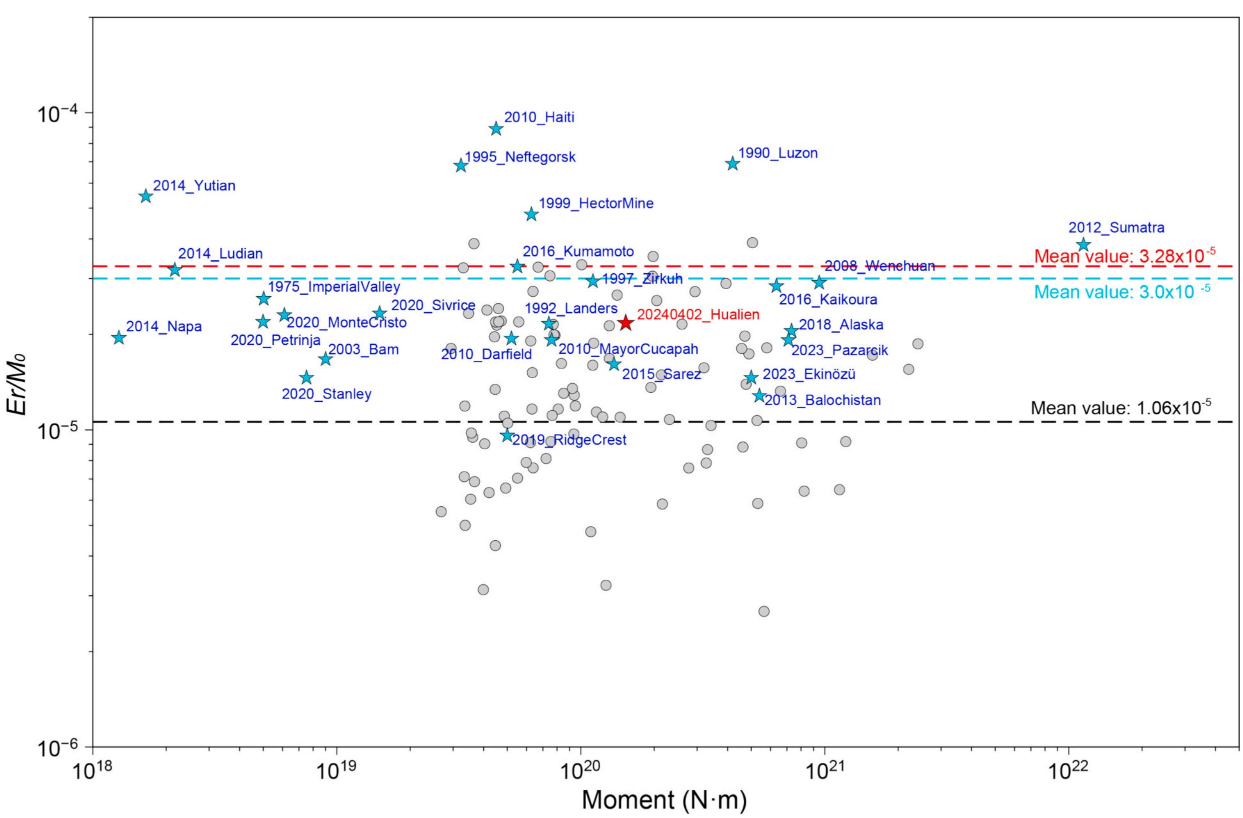

Fig. 9. The radiated energy/seismic moment value (E_r/M_0) for worldwide large complex earthquakes, and the mean value (3.0×10^{-5}) is indicated by a horizontal cyan dashed line. Cyan stars represent strike-slip events, and the red star marks the 2024 M_W 7.4 Hualien earthquake. The red and black dashed horizontal lines indicate the mean E_r/M_0 values for strike-slip events (Liu et al., 2023) and megathrust events (gray dots from Ye et al., 2016), respectively. (For interpretation of the references to colour in this figure legend, the reader is referred to the web version of this article.)

Xiong: Investigation, Formal analysis, Data curation. **Xiong Xiong:** Investigation, Funding acquisition, Formal analysis.

Declaration of competing interest

The authors declare that they have no known competing financial interests or personal relationships that could have appeared to influence the work reported in this paper.

Acknowledgments

We thank editor Gregory Houseman and one anonymous reviewer for their constructive comments. We thank Huihui Weng at Nanjing University for his helpful discussion of CFS calculation, thank Prof. Aitaro Kato at the University of Tokyo for sharing relocated aftershocks following the 2007 M_W 6.6 Chuetsu-oki Earthquake, and thank Keisuke Yoshida at Tohoku University for sharing relocated aftershocks following the 2008 M_W 6.9 Iwate-Miyagi earthquake. C. Liu was supported by the National Natural Science Foundation of China (No. 42222403) and the National Key Research and Development Program of China under grant 2022YFF0800703. T. Lay's earthquake research is supported by US National Science Foundation (Grant EAR1802364). X. Xiong was supported by MOST Special Fund from State Key Laboratory of Geological Processes and Mineral Resources, China University of Geosciences (MSFGPMR2024-502)

Appendix A. Supplementary material

Supplementary material related to this article can be found online at https://doi.org/10.1016/xxxxx

Data availability

All teleseismic body wave records can be obtained from the data management center of the Incorporated Research Institutions for Seismology (IRIS) (http://ds.iris.edu/wilber3/find_stations/11824102). Broadband radiated energy at teleseismic distances is available from the EQEnergy application of the IRIS (http://ds.iris.edu/spud/event/11824102). Strong motion seismograms were obtained from the Taiwan Seismological and Geophysical Data Management System (https://gdms.cwa.gov.tw/) and P-Alert Strong Motion Network (https://palert.earth.sinica.edu.tw/). Coseismic GNSS displacements are abtained from the Nevada Geodetic Laboratory (http://geodesy.unr.edu/). Strong ground shaking near the epicenter is from the Central Weather Administration Seismological Center of Taiwan (https://scweb.cwa.gov.tw/zh-tw/earthquake/shakemap/2024040307580972019). Moment Tensor catalog of aftershocks are available from the AutoBATS (https://tecdc.earth.sinica.edu.tw/FM/AutoBATS/). All slip models are available at: https://zenodo.org/records/18713654.

References

Aochi, H., Kato, A., 2010. Dynamic rupture of crosscutting faults: a possible rupture process for the 2007 M_W 6.6 Niigata-ken Chuetsu-Oki earthquake. J. Geophys. Res. Solid Earth 115 (B5). https://doi.org/10.1029/2009JB006556.

Cheloni, D., Famiglietti, N.A., Caputo, R., Tolomei, C., Vicari, A., 2024. A composite fault model for the 2024 M_W 7.4 Hualien earthquake sequence in eastern Taiwan inferred from GNSS and InSAR data. Geophys. Res. Lett. 51, e2024GL110255. https://doi.org/10.1029/2024GL110255.

Chen, C.Y., Lee, J.C., Chen, Y.G., Chen, R.F., 2014. Campaigned GPS on present-day crustal deformation in northernmost Longitudinal Valley preliminary results, Hualien Taiwan. Terr. Atmos. Ocean. Sci. 25 (3), 337–357. https://doi.org/10.3929/ethz-b-000085621.

Chen, K.H., Toda, S., Rau, R.J., 2008. A leaping, triggered sequence along a segmented fault: the 1951 M_L 7.3 Hualien-Taitung earthquake sequence in eastern Taiwan. J. Geophys. Res. Solid Earth 113 (B2). https://doi.org/10.1029/2007JB005048.

Chen, Y., Song, C., Li, Z., Chen, B., Yu, C., Hu, J.C., Peng, J., 2025. Preliminary analysis of landslides induced by the 3 April 2024 Mw 7.4 Hualien, Taiwan earthquake. Landslides 22 (5), 1551–1562.

Convers, J.A., Newman, A.V., 2011. Global evaluation of large earthquake energy from 1997 through mid-2010. J. Geophys. Res. 116, B08304. https://doi.org/10.1029/2010JB007928.

DeMets, C., Gordon, R.G., Argus, D.F., 2010. Geologically current plate motions. Geophys. J. Int. 181 (1), 1–80. https://doi.org/10.1111/j.1365-246X.2009.04491.x.

Dunham, E.M., Belanger, D., Cong, L., Kozdon, J.E., 2011. Earthquake ruptures with strongly rate-weakening friction and off-fault plasticity, part 2: nonplanar faults. Bull. Seismol. Soc. Am. 101 (5), 2308–2322.

Freed, A.M., 2005. Earthquake triggering by static, dynamic, and postseismic stress transfer. Annu. Rev. Earth Planet. Sci. 33 (1), 335–367. https://doi.org/10.1146/annurev.earth.33.092203.122505.

Fukuyama, E., 2015. Dynamic faulting on a conjugate fault system detected by near-fault tilt measurements. Earth Planets Space 67, 1–10. https://doi.org/10.1186/s40623-015-0207-1.

den Hartog, S.A.M., Thomas, M.Y., Faulkner, D.R., 2021. How do laboratory friction parameters compare with observed fault slip and geodetically derived friction parameters? Insights fomr the Longitudinal Valley Fault, Taiwan. J. Geophys. Res. Solid Earth 126, e2021JB022390. https://doi.org/10.1029/2021JB022390.

He, P., Liu, C., Wen, Y., Ding, K., 2024. Complex rupture features and triggering during the 2022 Chishang earthquake sequence in Eastern Taiwan estimated by InSAR, GPS, strong motion, and teleseismic waveform evidence. Seismol. Res. Lett. 95 (4), 2092–2104. https://doi.org/10.1785/0220230358.

Helmberger, D.V., 1974. Generalized ray theory for shear dislocations. Bull. Seismol. Soc. Am. 64 (1), 45–64. https://doi.org/10.1785/BSSA0640010045.

Hsu, Y.C., Chang, C.P., Yen, I.C., Huang, S.Y., Yen, J.Y., 2024. Investigating the structure under the Pingting Terrace from the co-seismic surface rupture of the 2022 Guanshan earthquake. Terr. Atmos. Ocean. Sci. 35 (1), 3.

Huang, H.H., Wang, Y., 2022. Seismogenic structure beneath the northern Longitudinal Valley revealed by the 2018-2021 Hualien earthquake sequences and 3-D velocity model. Terr. Atmos. Ocean. Sci. 33 (1), 17. https://doi.org/10.1007/s44195-022-00017-z.

Huang, H.-H., Wu, Y.-M., Song, X., Chang, C.-H., Kuo-Chen, H., Lee, S.-J., 2014. Investigating the lithospheric velocity structures beneath the Taiwan region by nonlinear joint inversion of local and teleseismic P wave data: slab continuity and deflection. Geophys. Res. Lett. 41, 6350–6357. https://doi.org/10.1002/2014GL061115.

Huang, M.H., Huang, H.H., 2018. The complexity of the 2018 M_W 6.4 Hualien earthquake in East Taiwan. Geophys. Res. Lett. 45 (24), 13–249. https://doi.org/10.1029/2018GL080821.

Ji, C., Wald, D.J., Helmberger, D.V., 2002. Source description of the 1999 Hector Mine, California, earthquake, part I: wavelet domain inversion theory and resolution analysis. Bull. Seismol. Soc. Am. 92 (4), 1192–1207. https://doi.org/10.1785/0120000916.

Ji, C., Helmberger, D.V., Wald, D.J., Ma, K.F., 2003. Slip history and dynamic implications of the 1999 Chi-Chi, Taiwan, earthquake. J. Geophys. Res. Solid Earth 108 (B9), 2412. https://doi.org/10.1029/2002JB001764.

Jian, P.R., Tseng, T.L., Liang, W.T., Huang, P.H., 2018. A new automatic full-waveform regional moment tensor inversion algorithm and its applications in the Taiwan area. Bull. Seismol. Soc. Am. 108 (2), 573–587.

Jian, P.R., Hung, S.H., Meng, L., 2019. Rupture behavior and interaction of the 2018 Hualien earthquake sequence and its tectonic implication. Seismol. Res. Lett. 90 (1), 68–77. https://doi.org/10.1785/0220180241.

Kaneko, Y., Lapusta, N., Ampuero, J.P., 2010. Spectral-element simulations of long-term fault slip: effect of low-rigidity layers on earthquake-cycle dynamics. J. Geophys. Res. Solid Earth 115 (B12). https://doi.org/10.1029/2010JB007581.

Kato, A., Sakai, S., Kurashimo, E., Igarashi, T., Iidaka, T., Hirata, N., Group for the Aftershock Observations of the 2007 Niigataken Chuetsu-oki Earthquake, 2008. Imaging heterogeneous velocity structures and complex aftershock distributions in the source region of the 2007 Niigataken Chuetsu-oki Earthquake by a dense seismic observation. Earth, Planets Space 60, 1111–1116. https://doi.org/10.1186/BF03353145.

King, G.C.P., Stein, R.S., Lin, J., 1994. Static stress changes and the triggering of earthquakes. Bull. Seismol. Soc. Am. 84 (3), 935–953.

Lacombe, O., Mouthereau, F., Angelier, J., Deffontaines, B., 2001. Structural, geodetic and seismological evidence for tectonic escape in SW Taiwan. Tectonophysics 333 (1–2), 323–345. https://doi.org/10.1016/S0040-1951(00)00281-X.

Lay, T., Ye, L., Bai, Y., Cheung, K.F., Kanamori, H., 2018. The 2018 M_W 7.9 Gulf of Alaska earthquake: multiple fault rupture in the Pacific plate. Geophys. Res. Lett. 45 (18), 9542–9551. https://doi.org/10.1029/2018GL079813.

Lee, J.-C., Angelier, J., Chu, H.-T., Yu, S.-B., Hu, J.-C., 1998. Plate-boundary strain partitioning along the sinistral collision suture of the Philippine and Eurasian plates: analysis of geodetic data and geological observation in southeastern Taiwan. Tectonics 17 (6), 859–871. https://doi.org/10.1029/98tc02205.

Lee, S.-J., Lin, T.-C., Liu, T.-Y., Wong, T.-P., 2019. Fault-to-fault jumping rupture of the 2018 M_W 6.4 Hualien earthquake in eastern Taiwan. Seismol. Res. Lett. 90 (1), 30–39. https://doi.org/10.1785/0220180182.

Lee, S.-J., Liu, T.-Y., Lin, T.-C., 2023. The role of the west-dipping collision boundary fault in the Taiwan 2022 Chihshang earthquake sequence. Sci. Rep. 13, 3552. https://doi.org/10.1038/s41598-023-30361-0.

Lin, K.C., Hu, J.C., Ching, K.E., Angelier, J., Rau, R.J., Yu, S.B., Huang, M.H., 2010. GPS crustal deformation, strain rate, and seismic activity after the 1999 Chi-Chi earthquake in Taiwan. J. Geophys. Res. Solid Earth 115 (B7). https://doi.org/10.1029/2009JB006417.

Liu, C., Lay, T., Wang, R., Taymaz, T., Xie, Z., Xiong, X., Erman, C., 2023. Complex multi-fault rupture and triggering during the 2023 earthquake doublet in southeastern

Türkiye. Nat. Commun. 14 (1), 5564. https://doi.org/10.1038/s41467-023-41404-5.
Liu, Z., Hu, J.C., Li, Z., Yu, C., Song, C., Wang, Z., Peng, J., 2025. New insights of the conjugate seismogenic structure in the northernmost Longitudinal Valley revealed by the 2024 Hualien (Taiwan) earthquake from geodetic and seismic observations. J. Geophys. Res. Solid Earth 130 (8), e2024JB031025.
Lo, Y.-C., Yue, H., Sun, J., Zhao, L., Li, M., 2019. The 2018 M_W6. 4 Hualien earthquake: dynamic slip partitioning reveals the spatial transition from mountain building to subduction. Earth Planet. Sci. Lett. 524, 115729. https://doi.org/10.1016/j.epsl.2019.115729.
Mai, P.M., Beroza, G.C., 2002. A spatial random field model to characterize complexity in earthquake slip. J. Geophys. Res. Solid Earth 107 (B11). ESE-10.
Michel, S., Avouac, J.P., Lapusta, N., Jiang, J., 2019. Pulse-like partial ruptures and high-frequency radiation at creeping-locked transition during megathrust earthquakes. Geophys. Res. Lett. 46 (24), 13665–13674. https://doi.org/10.1029/2019GL084817.
Robinson, D.P., Henry, C., Das, S., Woodhouse, J.H., 2001. Simultaneous rupture along two conjugate planes of the Wharton Basin earthquake. Science 292 (5519), 1145–1148.
Ruppert, N.A., Rollins, C., Zhang, A., Meng, L., Holtkamp, S.G., West, M.E., Freymueller, J.T., 2018. Complex faulting and triggered rupture during the 2018 M_W 7.9 offshore Kodiak, Alaska, earthquake. Geophys. Res. Lett. 45 (15), 7533–7541.
Shao, G., Li, X., Ji, C., Maeda, T., 2011. Focal mechanism and slip history of the 2011 M_W 9.1 off the Pacific coast of Tohoku Earthquake, constrained with teleseismic body and surface waves. Earth Planets Space 63, 559–564. https://doi.org/10.5047/eps.2011.06.028.
Shyu, J.B.H., Chen, C.F., Wu, Y.M., 2016. Seismotectonic characteristics of the northernmost Longitudinal Valley, eastern Taiwan: structural development of a vanishing suture. Tectonophysics 692, 295–308. https://doi.org/10.1016/j.tecto.2015.12.026.
Tang, C.-H., Lin, Y.N., Tung, H., Wang, Y., Lee, S.-J., Hsu, Y.-J., Shyu, J.B.H., Kuo, Y.-T., Chen, H.-Y., 2023. Nearby fault interactions with the double-vergence suture in eastern Taiwan during the 2022 Chishang earthquake sequence. Commun. Earth Environ. 4, 333. https://doi.org/10.1038/s43247-023-00994-0.
Tang, X., Guo, R., Li, L., Xu, Y., Xu, J., Zheng, Y., Sun, H., 2025. Earthquake interactions in eastern Taiwan: insight from the 2024 MW 7.3 Hualien Earthquake. Seismol. Res. Lett. 96 (1), 9–18.
Tsai, Y.B., 1986. Seismotectonics of Taiwan. Tectonophysics 125 (1–3), 17–37. https://doi.org/10.1016/0040-1951(86)90005-3.
Venkataraman, A., Kanamori, H., 2004. Observational constraints on the fracture energy of subduction zone earthquakes. J. Geophys. Res. Solid Earth 109, B05302. https://doi.org/10.1029/2003JB002549.
Wang, C.Y., Shin, T.C., 1998. Illustrating 100 years of Taiwan seismicity. Terr. Atmos. Ocean. Sci. 9, 589–614.
Wang, R., Lorenzo-Martín, F., Roth, F., 2006. PSGRN/PSCMP-a new code for calculating co-and post-seismic deformation, geoid and gravity changes based on the viscoelastic-gravitational dislocation theory. Comput. Geosci. 32 (4), 527–541.
Wetzler, N., Brodsky, E.E., Lay, T., 2016. Regional and stress drop effects on aftershock productivity of large megathrust earthquakes. Geophys. Res. Lett. 43 (23), 12–012.
Woessner, J., Jonsson, S., Sudhaus, H., Baumann, C., 2006. Probabilistic aftershock hazard mapping for large earthquakes in densely populated regions: the example of the 1992 Landers earthquake sequence. Bull. Seismol. Soc. Am. 96 (6), 2105–2117. https://doi.org/10.1785/0120050067.
Xie, X.-B., Yao, Z.-X., 1991. The faulting process of Tangshan earthquake inverted simultaneously from the teleseismic waveforms and geodesic deformation data. Phys. Earth Planet. Inter. 66 (3–4), 265–277. https://doi.org/10.1016/0031-9201(91)90081-R.
Xu, Y., Liu, Z., Tang, W., Wang, X., Han, S., Wang, X., Xiao, Y., Shang, J., Huang, L., Li, M., 2025. Rapid estimation of rupture directivity of the 2024 Mw 7.4 Hualien earthquake in the East China Sea (Taiwan region), China. Earthq. Res. Adv., 100411 https://doi.org/10.1016/j.eqrea.2025.100411.
Yang, Z., Chen, H., 2025. The rupture process of the Hualien M 7.3 sequence on April 3, 2024. Earthquake Res. Adv. 5 (1), 100333. https://doi.org/10.1016/j.eqrea.2024.100333.
Ye, L., Lay, T., Kanamori, H., Rivera, L., 2016. Rupture characteristics of major and great ($M_W \geq 7.0$) megathrust earthquakes from 1990 to 2015: 1. Source parameter scaling relationships. J. Geophys. Res. Solid Earth 121 (2), 826–844. https://doi.org/10.1002/2015JB012426.
Yen, J.Y., Lu, C.H., Dorsey, R.J., Kuo-Chen, H., Chang, C.P., Wang, C.C., Chang, W.Y., 2019. Insights into seismogenic deformation during the 2018 Hualien, Taiwan, earthquake sequence from InSAR, GPS, and modeling. Seismol. Res. Lett. 90 (1), 78–87. https://doi.org/10.1785/0220180228.
Yoshida, K., Hasegawa, A., Okada, T., Iinuma, T., 2014. Changes in the stress field after the 2008 M 7. 2 Iwate-Miyagi Nairiku earthquake in northeastern Japan. J. Geophys. Res. Solid Earth 119 (12), 9016–9030. https://doi.org/10.1002/2014JB011291.
Yoshida, K., Ueno, T., Koketsu, K., 2016. Complementary slip distribution and aftershock occurrence of the 2015 Gorkha, Nepal, earthquake. Earth Planets Space 68 (1), 1–7. https://doi.org/10.1186/s40623-016-0488-9.
Yu, S.B., Kuo, L.C., 2001. Present-day crustal motion along the Longitudinal Valley Fault, eastern Taiwan. Tectonophysics 333 (1–2), 199–217. https://doi.org/10.1016/S0040-1951(00)00275-4.
Yue, H., Lay, T., Koper, K.D., 2012. En échelon and orthogonal fault ruptures of the 11 April 2012 great intraplate earthquakes. Nature 490 (7419), 245–249. https://doi.org/10.1038/nature11492.
Zhang, H., Chen, J., Ge, Z., 2012. Multi-fault rupture and successive triggering during the 2012 M_W 8.6 Sumatra offshore earthquake. Geophys. Res. Lett. 39 (22).
Zhang, M., Liu, M., Feng, T., Wang, R., Zhu, W., 2022. LOC-FLOW: an end-to-end machine learning-based high-precision earthquake location workflow. Seismol. Res. Lett. 93 (5), 2426–2438. https://doi.org/10.1785/0220220019.
Zheng, A., Yu, X., Bai, C., Xu, W., Qian, J., Zhang, W., Chen, X., 2024. Thrust-dominated unilateral rupture of a blind listric fault associated with the 2024 Hualien earthquake. Sci. Rep. 14 (1), 31496.
Zhu, L., Rivera, L.A., 2002. A note on the dynamic and static displacements from a point source in multilayered media. Geophys. J. Int. 148 (3), 619–627. https://doi.org/10.1046/j.1365-246X.2002.01610.x.